IEEE Access
Multidisciplinary | Rapid Review | Open Access Journal

Received December 6, 2019, accepted January 6, 2020, date of publication January 10, 2020, date of current version January 29, 2020.

*Digital Object Identifier 10.1109/ACCESS.2020.2965653*

# Optimal Area-Product Model (OAPM) Based Non-Iterative Analytical Design Methodology for Litz-Wired High-Frequency Gapped-Transformer (LHFGT) in LLC Converters

**DANIYAL AHMED, (Student Member, IEEE), AND LI WANG, (Member, IEEE)**
Centre for More-Electric Aircraft Power System, Nanjing University of Aeronautics and Astronautics, Nanjing 211100, China

Corresponding author: Li Wang (liwang@nuaa.edu.cn)

This work was supported in part by the National Natural Science Foundation of China under Grant 51777092.

**ABSTRACT** In dc-dc LLC resonant converters, the Litz-wired high-frequency gapped-transformer (LHFGT) plays an important role, as it provides the necessary isolation, the required voltage-conversion, and the desired magnetizing inductance ($L_m$) for efficient converter operation. Since the LHFGT makes a significant contribution to the overall converter weight and size, so the converter designers must rely on complicated and advanced optimization techniques, with a large number of iterations, for its design. This dependence is due to the shortcomings in the conventional analytical modeling techniques for optimal size-selection of the core and winding in the LHFGT. Hence, this manuscript proposes an optimal area-product ($A_{prod}$) model (OAPM)-based non-iterative LHFGT design methodology that maximizes the efficiency and power density, minimizes the losses and volume, integrates the $L_m$, and maintains the temperature-rise within limits. The method takes into consideration the LLC circuit parameters, the Litz-wire strand-radius ($r_s$), the core material and geometrical parameters, the excitation-waveform shape, the stored energy due to core-airgap, and the peak flux-density ($B_{pk}$) inside the core. The accuracy improvement is attained through the proposal of accurate $A_{prod}$-based core-geometry features estimation (ACGFE) models and by keeping in view the interdependency between the transformer-design parameters (TDPs). The optimized design is obtained in a single iteration, based on the proposed OAPM, the proposed optimal $r_s$ selection model, and the proposed optimal TDPs' models. The proposed design routine is validated through the analytical and experimental results of a prototype LHFGT for a 200W-110kHz-400VDC/12VDC LLC resonant converter.

**INDEX TERMS** Area-product based core-geometry features estimation (ACGFE) parameters, Litz-wired high-frequency gapped-transformer (LHFGT), LLC resonant converter, optimal area-product model (OAPM), optimal Litz-wire strand-radius selection (LSS) model, optimal transformer-design parameters' models (OTDPMs), optimization.

## I. INTRODUCTION

The LLC resonant converters are the resonant converters having the highest efficiency with wide-ranging voltage-gain. This makes them the most preferred converters for use in the dc-dc isolation stage of the switch-mode power supplies (SMPS) [1]–[6]. With advancements in the area of power electronics, the trend is towards high efficiency and high power density designs [6]–[9]. In the LLC converters, the main contributor to the weight and volume is the Litz-wired high-frequency gapped-transformer (LHFGT). The LHFGT plays a vital role in providing the necessary voltage-isolation, the required voltage-conversion, and the desired magnetizing-inductance ($L_m$) for efficient converter operation. The core air-gap ($g_{cr}$) in LHFGT enables the integration of $L_m$ for the realization of zero-voltage-switching, whereas, the Litz-wire contributes to minimizing the high-frequency factor (HFF) of the winding loss ($P_{cu}$) [9]–[11].

In the LHFGT, the addition of $g_{cr}$ results in the energy-storage similar to an inductor, in addition to the power-transfer like that of a conventional transformer (CT).

The associate editor coordinating the review of this manuscript and approving it for publication was Narsa T Reddy.

This $g_{cr}$ also causes the relative permeability ($\mu_r$) of the core to be changed [11], [12]. Furthermore, unlike the CT, in LHFGT, only a part of the input current or the resonant current ($I_{res}$), i.e., the magnetizing current ($I_{mg}$), is responsible for the core magnetization and the flux linkage, whereas, the $I_{res}$ as a whole is responsible for the primary winding-loss ($P_{cup}$) of the LHFGT [12]. Therefore, as a result of these distinguishing features between the CT and the LHFGT, the LLC circuit parameters ($L_m$, $I_{res}$, and $I_{mg}$), the $g_{cr}$, the stored energy, and the modified $\mu_r$ called the effective-permeability ($\mu_e$), all need to be incorporated in the core and winding size-selection (CWSS) process for the LHFGT.

In LHFGT design optimization, the maximization of the efficiency ($\eta_t$) and the power-density ($\psi_{pd}$) requires the minimization of the total losses ($P_t$) and the volume ($V_t$) of the LHFGT while keeping the temperature-rise ($\Delta T_r$) within limits. This optimization is a challenging task [7], [8] since the $P_t$ varies nonlinearly with the decrease in $V_t$. Therefore, the converter designers go through time & resource consuming, cumbersome, and complicated multi-objective optimization techniques that require a large number of iterations [2], [7]–[9], [13]–[21]. These techniques result in a large number of solutions called Pareto-optimal solutions. Furthermore, these methods do not incorporate the relationship between the transformer-design parameters (TDPs), taken as the optimization-variables (OVs). In each iteration, the algorithm assigns new values to the OVs from a predefined value-range, and the resulting transformer, if feasible, is considered as a Pareto-optimal solution. The process continues until the complete range of all OVs has been covered. All OVs are assigned values independently, that is a reason for requiring such a large number of iterations for optimality search. These solutions may be two-million in case of a brute-force-optimization methodology [18], [19], or forty-thousand in case of the genetic-algorithm [7]. The designers have to select the final design out of these many solutions; this itself is another difficult task.

The high reliance on these lengthy iterative techniques is due to the inability of the conventional analytical CWSS models to provide an optimal design of the LHFGT. These models include the area-product ($A_{prod}$) model [22], [23], and the core-geometrical factor ($K_G$) model [24], [25]. For any core size, the $A_{prod}$ value can be obtained using the values of the core area ($A_{cr}$) and the winding window-area ($A_w$) as, $A_{prod} = A_w \cdot A_{cr}$, whereas, the $K_G$ value, depending on the $A_{cr}$, the $A_w$, and the winding mean-length-turn ($l_w$), can be obtained as, $K_G = A_w \cdot A_{cr}^2/l_w$. These two CWSS models evaluate the power-handling ability of the transformer cores and choose a specific sized core based on the obtained values. Among the two models, the $A_{prod}$ is the most commonly used and preferred model, with many ferrite core manufacturers [26]–[29] providing its value along with the core dimensions in the datasheets. On the other hand, the calculation of the $K_G$ value requires additional information regarding the core-bobbin and the $l_w$, which is usually not directly provided in the datasheets [27]–[30].

In order to utilize the benefit of these $A_{prod}$ and $K_G$ CWSS models, researchers have combined these models with brute-force iterative techniques to reduce the number of iterations for obtaining the optimal design. The $A_{prod}$ model has been integrated into the iterative methods proposed in [11], [15], [31]–[36], whereas the $K_G$ model has been employed in [14], [37]. Although, these improved techniques with the incorporation of the CWSS models result in a feasible design with reduced iterations, however, the limitations of these conventional $A_{prod}$ and $K_G$ models reduce the overall applicability. The obtained feasible design may or may not be an optimal design due to several drawbacks associated with these CWSS models that include,

1) LLC circuit parameters, energy storage in $g_{cr}$, $\mu_e$, and $\Delta T_r$ have not been incorporated in the formulation of these models.
2) Core-material parameters have also not been considered in these CWSS models. Even though the core material greatly influences the $P_t$ and $V_t$ of the transformer, as shown in 8].
3) Assumed values for important TDPs are used. The $K_G$ model [24] assumes the values for voltage regulation ($V_r$), $\eta_t$, and $B_{pk}$, whereas the $A_{prod}$ model [22], [23] requires assumed value for $B_{pk}$. In [23], assumed value for current density ($J_w$) has also been used for the $A_{prod}$ model. Furthermore, the interdependency between these TDPs is not considered while assuming their values.
4) Inaccurate Litz-wire strand-radius selection (LSS) criterion is employed where the strand-radius ($r_s$) is selected using heuristic techniques [20], [24], [38]–[41] based on the nominal switching frequency ($f_s$) and the skin-depth ($\delta_{fs}$).

In order to address some of the above-highlighted deficiencies, the authors in [11], [23], [36] made a few improvements in these $A_{prod}$ and $K_G$ CWSS models. In [23], the authors improved the $K_G$ model by incorporating the resonant circuit parameters ($L_m$, $I_{res}$, and $I_{mg}$). However, the improved method still has limited applicability due to several reasons. Firstly, the model does not consider the $\Delta T_r$ limit, and secondly, it still requires assumed values for $V_r$, $\eta_t$, and $B_{pk}$. Furthermore, the model is dependent on iterative techniques for optimization. In [36], the authors have put efforts in incorporating the $\Delta T_r$ limit in the $A_{prod}$ model-formulation with the help of core-geometry features estimation (CGFE) models. These CGFE models estimate the value of geometry-features (GFs) such as core volume ($V_{cr}$), winding volume ($V_w$), and surface-area ($A_{srf}$), from the $A_{prod}$ value. The CGFE models in [36] have been proposed based on the dimensions of the $A_{cr}$ and the $A_w$ for E-shaped cores. These models require the cores to have a rectangular central-limb and assume that the dimensions of the side-limbs are half to those of the central-limb; thereby limiting its validity to only E-shaped and similar cores. These CGFE models, therefore, also limit the scope of the $A_{prod}$ CWSS model proposed in [36]. Also, this CWSS model [36] does not consider

the LLC circuit parameters, the energy storage in $g_{cr}$, and the $\mu_e$ making it unsuitable for LHFGT design in resonant converters.

As an improvement over the CWSS models in [23], [36], and the conventional models in [22]–[24], the authors in [11] have reported a benchmark method based on $A_{prod}$ model. The $A_{prod}$ model in [11] has been formulated by taking into consideration the LLC circuit parameters, the energy storage in $g_{cr}$, the $\mu_e$, and the $\Delta T_r$ limit. However, this model still has the following limitations:

1) The CWSS is an iterative process, and the designed LHFGT based on this model may be considered as a feasible solution but not the optimal solution. The maximization of $\eta_t$ and $\psi_{pd}$ or the minimization of $P_t$ and $V_t$ have not been considered during core-size selection or while selecting $r_s$.
2) Assumed values for important TDPs that include, the $B_{pk}$, and the core loss ($P_{fe}$) to $P_{cu}$ ratio, are used with no consideration to their interdependency. Also, the $P_{cup}$ is estimated based on the assumed $P_{fe}$ to $P_{cu}$ ratio value. This estimated $P_{cup}$ and the assumed$B_{pk}$ are later used for calculating the $\mu_{e,}$ and the primary-winding turns ($N_p$). Thus, these assumptions and the estimation of $P_{cup}$ make the entire design method weak with questionable accuracy.
3) The $A_{prod}$ model formulation is based on the transformer-cores' geometrical analysis (CGFE models) of [22] that has poor accuracy. These geometrical models in [22] use the same constant CGFE parameter-values for all core shapes thus resulting in an inaccurate estimation of the geometrical features.
4) The core-material parameters are not considered during the $A_{prod}$ model formulation.

In [42], the authors have proposed an optimal $B_{pk}$ model, based on which the LHFGT may be designed with minimized $P_t$ and $V_t$; however, the CWSS methodology employed is the same as the benchmark [11]. Moreover, the proposed $B_{pk}$ model is also based on the CGFE models of [22]. Although the proposed model [42] itself has merit, however, the drawbacks associated with the benchmark CWSS method in [11] and the CGFE models in [22], limit the applicability of [42]. This shows that there is a dire need for an improved analytical CWSS methodology for LHFGT in LLC converters that can overcome all the existing shortcomings.

Keeping the drawbacks of both the iterative optimization techniques and the CWSS analytical models in view, this paper proposes an improved $A_{prod}$ based methodology for LHFGT design in LLC converters with *main contributions* as stated below:

1) An improved optimal $A_{prod}$ model (OAPM)-based non-iterative analytical design methodology for CWSS of LHFGT in LLC converters is proposed. The aim is to maximize the $\eta_t$ and $\psi_{pd}$, minimize the $P_t$ and $V_t$, integrate the $L_m$, and maintain the $\Delta T_r$ within limits. The objectives are achieved with an improvement of above 30% in the $P_t$ and $V_t$ product ($P_t \cdot V_t$) as compared to the benchmark [11].
2) The accuracy improvement is achieved through the proposal of accurate $A_{prod}$-based core-geometry features estimation (ACGFE) models and by keeping in view the interdependency between the TDPs. The proposed ACGFE models are formulated based on the dimensions of the core's central & side limbs, the limb junctions, and the bobbin. Separate ACGFE parameter-models are proposed for cores having cylindrical and rectangular central-limbs, ensuring estimation of the GFs for different core shapes with high accuracy.
3) An optimal LSS model, based on the $f_s$ and the $\delta_{fs}$, is proposed for minimizing the $P_{cu}$ of the LHFGT. The model is formulated by analyzing the relationship between the Litz-wire shape, the $g_{cr}$, and the HFF.
4) The proposed models for the TDPs and the OAPM are formulated by incorporating the LLC circuit parameters, the optimal LSS model, the core material parameters, the proposed ACGFE models, the square excitation-waveform shape in LLC converters, the stored energy due to $g_{cr}$, and the overall optimization aim.
5) The optimized design of LHFGT is obtained, in a single iteration, based on the proposed OAPM, the proposed optimal LSS model, and the proposed optimal TDPs' models (OTDPMs).

In this paper, Section-II presents the formulation of the proposed ACGFE models, the proposed optimal LSS model, the proposed OTDPMs, and the proposed OAPM. Afterward, in Section-III, the proposed non-iterative optimal design methodology is presented, based on the models of Section-II, followed by the analytical design results. The method is proven through comparison with the benchmark method [11], the brute-force iterative optimization, the genetic algorithm (GA)-based optimization [7], as well as, the FEM simulations. The criteria for the method to be non-iterative is also discussed here. Later, in Section-IV, experimental results, by integrating the prototype LHFGT with the LLC converter, validate the design. In the end, the paper is concluded in Section-V.

## II. THE PROPOSED DESIGN-MODELS' FORMULATION

### A. THE ACCURATE ACGFE MODELS

The ACGFE models are mathematical models that estimate the GFs of a transformer by extracting information from the $A_{prod}$ value. The GFs that may be estimated from the $A_{prod}$ include, $V_{cr}$, $V_w$, $A_{srf}$, $A_{cr}$, $A_w$, $l_w$, and core magnetic-path-length ($l_{cr}$). The ACGFE models, based on the models in [11], [22], [36], have the following generic form:

$$X = k_x A_{prod}^{y} \tag{1}$$

In (1), $X$ represents the GF being extracted from the $A_{prod}$ value, $k_x$ represents the ACGFE parameter or the scaling factor (dimensionless), and $y$ is used for matching the

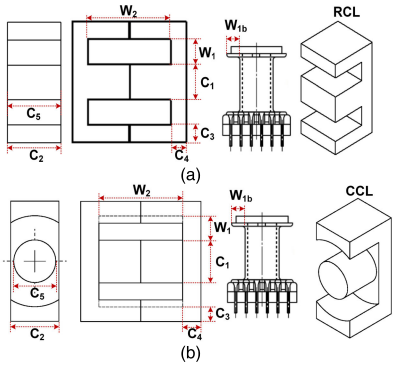


**FIGURE 1.** (a) RCL shaped EE core. (b) CCL shaped EER core. Core dimensions (in both (a) & (b)): $W_1$ (Width of winding-window-area), $W_2$ (Height of winding-window-area), $W_{1b}$ (Width of winding-area in Bobbin), $C_1$ (Width of central-core-limb), $C_2$ (Depth of side-core-limbs), $C_3$ (Width of side-core-limbs), $C_4$ (Height of core-limbs-junction), $C_5$ (Depth of central-core-limb).

dimensions of the $A_{\text{prod}}$ with those of the $X$. In the design process, these models can be used in the formulation of almost all TDPs and objective-functions, i.e., $P_{\text{cu}}$, $P_{\text{fe}}$, $B_{\text{pk}}$, $J_{\text{w}}$, $\mu_{\text{e}}$, $V_{\text{t}}$, $\eta_{\text{t}}$, and $\psi_{\text{pd}}$, etc., making these models independent of the physical dimensions of the core. This utility also allows the CWSS methodology to avoid going through iterative loops for verification of TDPs bounds, as being done in the conventional analytical design methods [22]–[24]. The existing approximate ACGFE models [11], [22], [36], can be used for interpreting the trends and trade-offs in the transformer shape with changing $A_{\text{prod}}$; however, for accurate transformer design and optimization, these models may not be employed. Therefore, the accuracy of these ACGFE models plays a vital role in the overall accuracy of the CWSS design methodology.

In this paper, the authors have conducted a detailed dimensional analysis of transformers with concentric windings around the central core-limb. Various transformer core-shapes, such as PQ, EE, EER, and ETD, have been analyzed. These core shapes have been categorized into cores having the rectangular central-limbs (RCL) and cores having the cylindrical central-limbs (CCL). The central-limb is the core-limb on which the concentric transformer-windings have been wound. It has been concluded that the GFs of the transformers can be represented with enough accuracy (average error of less than 5%), using the dimensions as labeled in Fig. 1. In order to obtain the proposed mathematical accurate ACGFE models, the dimensions (in Fig. 1) are firstly converted to dimensionless ratios or per-unit values by considering the longest dimension as the base-value (in this case, $W_2$). The ratios are:

$$\begin{aligned} &W_{1pu} = W_1/W_2; \quad W_{2pu} = W_2/W_2 = 1; W_{1bpu} = W_{1b}/W_2; \\ &C_{1pu} = C_1/W_2; \quad C_{2pu} = C_2/W_2; C_{3pu} = C_3/W_2; \\ &C_{4pu} = C_4/W_2; \quad \text{and } C_{5pu} = C_5/W_2; \end{aligned} \tag{2}$$

Using the fundamental definitions of GFs, the per-unit ratios in (2), and the generic form (1), the following proposed ACGFE models, (3) to (9), have been formulated.

$$V_{\text{cr}} \text{ ACGFE model} : V_{cr} = k_{cr} A_{prod}^{3/4} \tag{3}$$

where (for RCL-shapes),

$$k_{cr} = \left(2W_{1pu} + \sqrt{C_{3pu}^2 + C_{4pu}^2} + \sqrt{C_{1pu}^2 + C_{4pu}^2} + 2\right) \Big/ \left((W_{1pu})^{\frac{3}{4}} (C_{1pu} C_{5pu})^{\frac{-1}{2}}\right)$$

and (for CCL-shapes),

$$k_{cr} = \left(2W_{1pu} + \sqrt{C_{3pu}^2 + C_{4pu}^2} + \sqrt{C_{1pu}^2 + C_{4pu}^2} + 2\right) \Big/ \left((\frac{\pi}{4} W_{1pu})^{\frac{3}{4}} (C_{1pu} C_{5pu})^{\frac{-1}{2}}\right)$$

$$V_{\text{w}} \text{ ACGFE model} : V_w = k_w A_{prod}^{3/4} \tag{4}$$

where (for RCL-shapes),

$$k_w = 2W_{1pu}^{\frac{1}{4}} (2W_{1pu} + C_{1pu} + C_{5pu}) \Big/ \left[C_{1pu} C_{5pu}\right]^{\frac{3}{4}}$$

and (for CCL-shapes),

$$k_w = \left(64\pi W_{1pu}\right)^{\frac{1}{4}} \left(2W_{1pu} + C_{1pu} - W_{1bpu}\right) \Big/ \left[C_{1pu} C_{5pu}\right]^{\frac{3}{4}}$$

$$A_{\text{srf}} \text{ ACGFE model} : A_{srf} = k_{srf} A_{prod}^{1/2} \tag{5}$$

where (for RCL-shapes),

$$k_{srf} = \frac{\begin{array}{l} 4W_{1pu}(W_{1pu} + C_{4pu} + 1) + C_{1pu}(2W_{1pu} + 2C_{4pu} + 1) \\ +2C_{2pu}(C_{3pu} + C_{4pu}) + 2C_{3pu}(1 + 2C_{4pu}) + C_{5pu}(2W_{1pu} + C_{1pu} + 1) \end{array}}{0.5[W_{1pu} C_{1pu} C_{5pu}]^{1/2}}$$

and (for CCL-shapes),

$$k_{srf} = \frac{\begin{array}{l} 4W_{1pu}(W_{1pu} + C_{4pu} + 1) + C_{1pu}(2W_{1pu} + 2C_{4pu} + 1) \\ +2C_{2pu}(C_{3pu} + C_{4pu}) + 2C_{3pu}(1 + 2C_{4pu}) + C_{5pu}(2W_{1pu} + C_{1pu} + 1) \end{array}}{0.25[\pi W_{1pu} C_{1pu} C_{5pu}]^{1/2}}$$

$$A_{\text{cr}} \text{ ACGFE model} : A_{cr} = k_{Acr} A_{prod}^{1/2} \tag{6}$$

where (for RCL-shapes), $k_{Acr} = \left[C_{1pu} C_{5pu} / W_{1pu}\right]^{1/2}$
and (for CCL-shapes), $k_{Acr} = \left[(0.25\pi C_{1pu} C_{5pu}) / W_{1pu}\right]^{1/2}$

$$A_{\text{w}} \text{ ACGFE model} : A_w = k_{Aw} A_{prod}^{1/2} \tag{7}$$

where (for RCL-shapes), $k_{Aw} = \left[W_{1pu} / (C_{1pu} C_{5pu})\right]^{1/2}$ and (for CCL-shapes), $k_{Aw} = \left[W_{1pu} / (0.25\pi C_{1pu} C_{5pu})\right]^{1/2}$

$$l_{\text{cr}} \text{ ACGFE model} : l_{cr} = k_{MPL} A_{prod}^{1/4} \tag{8}$$

where (for RCL-shapes),

$$k_{MPL} = (2W_{1pu} + \sqrt{C_{3pu}^2 + C_{4pu}^2} + \sqrt{C_{1pu}^2 + C_{4pu}^2} + 2) \Big/ [W_{1pu} C_{1pu} C_{5pu}]^{1/4}$$

and (for CCL-shapes),

$$k_{MPL} = (2W_{1pu} + \sqrt{C_{3pu}^2 + C_{4pu}^2} + \sqrt{C_{1pu}^2 + C_{4pu}^2} + 2) \Big/ [0.25\pi W_{1pu} C_{1pu} C_{5pu}]^{1/4}$$

$$l_{\text{w}} \text{ ACGFE model} : l_w = k_{MLT} A_{prod}^{1/4} \tag{9}$$

where (for RCL-shapes),

$$k_{MLT} = 2(2W_{1pu} + C_{1pu} + C_{5pu}) \Big/ [W_{1pu} C_{1pu} C_{5pu}]^{1/4}$$

**TABLE 1. ACGFE parameter values for standard ferrite-cores.**

| Core Shape | $k_{Acr}$ | $k_{Aw}$ | $k_{MPL}$ | $k_{MLT}$ | $k_{srf}$ | $k_{cr}$ | $k_{w}$ |
|---|---|---|---|---|---|---|---|
| PQ | 0.974 | 1.026 | 6.285 | 5.659 | 35.818 | 6.669 | 5.807 |
| ETD | 0.746 | 1.341 | 7.484 | 5.313 | 40.748 | 5.582 | 7.123 |
| EER | 0.737 | 1.356 | 7.612 | 5.104 | 40.312 | 5.613 | 6.922 |
| EE | 0.699 | 1.430 | 6.767 | 6.298 | 39.123 | 4.732 | 9.006 |

and (for CCL-shapes),

$$k_{MLT} = (4\pi^3)^{1/4}(2W_{1pu} + C_{1pu} - W_{1bpu}) \Big/ [W_{1pu}C_{1pu}C_{5pu}]^{1/4}$$

The ratios in (2) can easily be obtained using any supplier datasheet for transformer cores. The values for the proposed ACGFE parameters of (3) to (9), for a few standard ferrite cores, calculated using the Ferroxcube datasheet have been shown in Table 1. The GF values for $A_{srf}$, $V_{cr}$, and $V_{w}$, calculated using the proposed ACGFE models (3) to (5), have been compared with the GF values obtained using the CGFE models in [11] & [22] (both use the same models), and the Ferroxcube-datasheet, for accuracy validation. This comparison has been presented in Fig. 2 for EE, PQ, ETD, and EER shapes. It can be seen from Fig. 2 that the proposed ACGFE models result in an accurate estimation of the GFs.

### B. THE OPTIMAL LSS MODEL

In this paper, an optimal LSS model is proposed in order to minimize the HFF of the $P_{cu}$ in the LHFGT. The Litz-wire $r_s$ plays an essential part in minimizing the HFF by reducing various high-frequency effects, which include the skin-effect, the proximity-effect, and the fringing-effect at the strand, bundle, and layer levels. Therefore, in order to select suitable $r_s$ for minimized HFF in LHFGT, the relationship between $f_s$, $r_s$, $g_{cr}$, and $\delta_{fs}$ have been analyzed through following 3D eddy FEM simulations in ANSYS Maxwell.

#### 1) EFFECT OF TWISTING ON HFF

In this simulation, the effect of change in twists per turn on the HFF over an $f_s$ range of 1Hz to 1MHz has been analyzed. The FEM models of a single round conductor-based winding and 02-strands-based Litz-wire winding with various twists/turn have been simulated. The winding consists of a single-layer, five-turns, coreless winding with the Litz-wire having $r_s$ of 0.2mm. The HFF results have been plotted against the ratio of $r_s$ to $\delta_{fs}$, instead of $f_s$, for the purpose of analyzing the relationship between the HFF and the $r_s$. These simulations aim to identify the upper limit of the ratio $r_s/\delta_{fs}$ for which the HFF is approximately equal to 1. The results have been plotted in Fig. 3(a) and the FEM models have been shown in Fig. 3(b). The FEM results exhibit that the effect of change in twists/turn is minimal with HFF approximately equal to 1, for the $f_s$ range where the ratio $r_s/\delta_{fs} \leq 0.5$.

#### 2) EFFECT OF CORE AIR-GAP ON HFF

The effect of change in $g_{cr}$ on the HFF is analyzed using the 3D quarter FEM model of a basic LHFGT having Litz-wire windings with 02-strands, 16-twists/turn, 0.2mm $r_s$, and

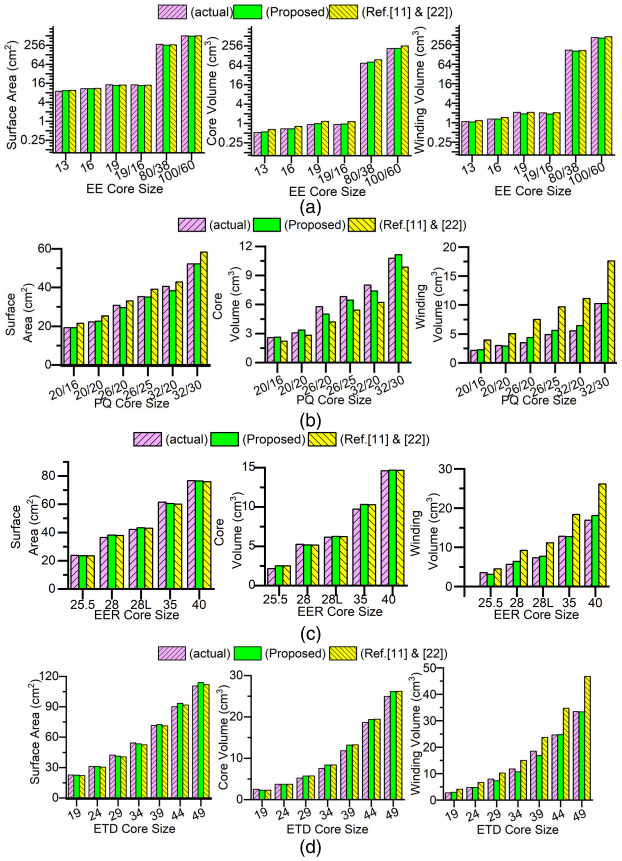


**FIGURE 2. GF values comparison for $A_{srf}$, $V_{cr}$, and $V_{w}$ of different core shapes obtained using the proposed ACGFE models, the models in [11] & [22], and the Ferroxcube datasheets. (a) EE core. (b) PQ core. (c) EER core. (d) ETD core. For all core shapes, the CGFE model of [11] & [22] show over-estimated or under-estimated results, except for the EE-shaped core (where the results are approximately the same).**

7:7 concentric turns wound over EER28 core. The $g_{cr}$ is varied from 0mm to 1.5mm, and the HFF results are presented for each $g_{cr}$ over the $f_s$ range of 1Hz to 1MHz. The basic LHFGT model has been designed, keeping in view the aim of the simulations. The FEM model exhibits all the effects (skin, proximity, and fringing effects) that constitute the HFF; hence, the simulation results convey a reliable and comprehensive criterion for minimization of HFF with respect to the ratio $r_s/\delta_{fs}$. The aim of this simulation is also to identify the upper limit of the ratio $r_s/\delta_{fs}$ for which the HFF is approximately equal to 1. The results have been plotted in Fig. 3(c) and the FEM model has been shown in Fig. 3(d). The FEM results exhibit that the effect of change in $g_{cr}$ is minimal with HFF approximately equal to 1, for the $f_s$ range where the ratio $r_s/\delta_{fs} \leq 0.5$.

#### 3) HFF RESPONSE OF LITZ-WIRE WINDING IN 200W LHFGT (VERIFICATION OF 1ST AND 2ND SIMULATIONS)

A 200W LHFGT 3D-quarter model, designed for 400VDC to 12VDC LLC converter, has been simulated in ANSYS Maxwell to analyze the relationship between $f_s$, $r_s$, $g_{cr}$, and $\delta_{fs}$, and for the verification of the results of the first and second simulations. The FEM model, shown

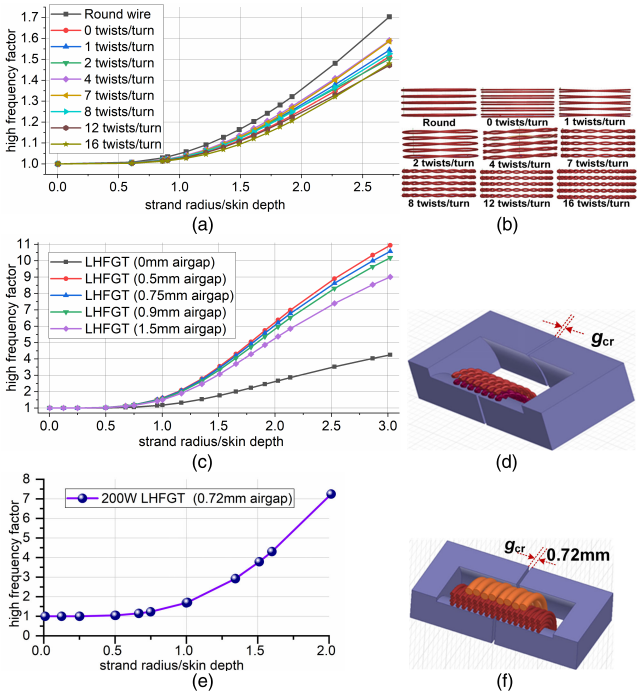


**FIGURE 3.** ANSYS Maxwell 3D Eddy Simulation results showing effects of change in $f_s$, $r_s$, $g_{cr}$, and $\delta_{fs}$ on HFF. (a) Effect of change in twists/turn and $r_s/\delta_{fs}$ on HFF. (b) Round and Litz-wire winding (coreless, 05-turns, 01-layer, $r_s = 0.2$mm) FEM models with various twists/turn used in simulation results of Fig. 3(a). (c) Effect of change in $g_{cr}$ and $r_s/\delta_{fs}$ on HFF. (d) Quarter 3D LHFGT FEM model used in simulation results of Fig. 3(c). (e) Effect of change in $f_s$ on HFF in actual 200W LHFGT. (f) Quarter 3D FEM model of 200W LHFGT used in simulation results of Fig. 3(e).

in Fig. 3(f), comprises of EER28 core with 32:2:2 turns-based Litz-wire concentric-windings having 02-untwisted strands/turn, 0.32mm primary $r_s$, 0.645mm secondary $r_s$, and 0.72mm $g_{cr}$. The 3D eddy simulations are run over an $f_s$ range of 1Hz to 1MHz, as shown in Fig. 3(e), respectively. The obtained results verify that the HFF is approximately equal to 1 and minimized for the $f_s$ range where the ratio $r_s/\delta_{fs} \leq 0.5$.

A conclusion can be drawn from the afore-mentioned simulation-results that, in order to minimize the HFF in the LHFGT design, the $r_s$ needs to be chosen such that the ratio $r_s/\delta_{fs} \leq 0.5$ at the desired $f_s$ value. Furthermore, in order to avoid any boundary-value uncertainties, a smaller $r_s$ may be chosen such that,

$$r_s \leq \delta_{fs}/4 \tag{10}$$

This conclusion may be considered as the necessary condition for HFF minimization. In LHFGT, according to [43], the HFF also depends on the turns/layer ($N_l$), the strands/turn ($S_t$), the copper-area/turn ($A_{cu-t}$), and the maximum breadth of the winding-layer ($b_l$), that is,

$$HFF = 1 + (\pi S_t N_l)^2 (2 \times r_s)^6 \Big/ (192 \times \delta_{fs}^4 b_l^2) \tag{11}$$

The $b_l$ for a concentric-winding wound on the central limb of the ferrite core is the height of the winding-window area. Now, (11) can be modified to obtain another condition for the selection of $r_s$ with respect to the desired $f_s$. Since $S_t = A_{cu-t}/\pi r_s^2$, therefore,

$$HFF = 1 + A_{cu-t}^2 N_l^2 r_s^2 \Big/ (3\delta_{fs}^4 b_l^2) \tag{12}$$

Also, the minimized HFF may be considered as HFF = 1 in an ideal case, or HFF $\leq$ (1+10%) in real applications, where 10% is the permissible error margin. If this margin is $\varepsilon_{HFF}$ with a value between 0.1% to 10%, then,

$$HFF = 1 + A_{cu-t}^2 N_l^2 r_s^2 \Big/ (3\delta_{fs}^4 b_l^2) \leq 1 + \varepsilon_{HFF} \tag{13}$$

$$\Rightarrow r_s \leq \sqrt{3\varepsilon_{HFF}}\,\delta_{fs}^2 b_l \Big/ (A_{cu-t} N_l) \tag{14}$$

Equation (14) may be considered as the second condition that needs to be satisfied to ensure the minimization of the HFF. Therefore, combining both (10) and (14) leads to the desired sufficient condition for which the HFF may be considered as minimized. Hence, we have,

$$r_s = \min\left[\, \delta_{fs}/4 \;,\; \sqrt{3\varepsilon_{HFF}}\,\delta_{fs}^2 b_l \Big/ (A_{cu-t} N_l) \,\right] \tag{15}$$

Equation (15) is the proposed optimal LSS model that chooses the $r_s$ in LHFGT such that the HFF is minimized. This model (15) selects the smaller of the two $r_s$ calculated using (10) and (14), thereby satisfying both criteria.

### C. THE OPTIMAL TDP MODELS (OTDPMs)

In order to select the optimal core and winding for the LHFGT, the models that assign the values to the TDPs, i.e., $B_{pk}$, $J_w$, $\mu_e$, $N_p$, and $g_{cr}$, all have been formulated, keeping in view the LLC circuit parameters, the optimal LSS model, the core material parameters, the ACGFE models, the square excitation-waveform shape in LLC converters, the stored energy due to $g_{cr}$, and the overall optimization aim, as follows:

#### 1) THE OPTIMALITY CONDITION

In this paper, the important optimization objectives, that are being targeted, include maximizing $\eta_t$ and $\psi_{pd}$, minimizing $P_t$ and $V_t$, integrating $L_m$ in primary of the LHFGT, and maintaining the $\Delta T_r$ within limits. These all objectives are interrelated; the minimization of $P_t$ results in the maximization of $\eta_t$, and similarly, the minimization of $V_t$ results in the maximization of $\psi_{pd}$. However, the reduction in $V_t$ may increase $P_t$, and hence reduction in $\eta_t$ as well. Also, $V_t$ and $\Delta T_r$ are inversely related, and integrating $L_m$ requires a specific $N_p$ leading to fixed $V_w$. The achievement of all these objectives simultaneously may be considered as a multi-objective optimization or Pareto-optimization. These relationships can be understood from the following equations.

The $P_t$ can be represented in terms of the total thermal loss due to convection ($P_{TH}$) using Newton's law of cooling [44] as,

$$P_t = P_{fe} + P_{cu} = P_{TH} = h_t \Delta T_r A_{srf} \tag{16}$$

where, $h_t$ is the coefficient of heat-transfer (typically 10W / ($m^2$°C) for natural-convection). By using (3) to (5)

in (16), $V_t$ can be represented in terms of $P_t$ as follows,

$$V_t = V_{cr} + V_w = (k_{cr} + k_w)\, P_t^{3/2} \Big/ \left(h_t k_{srf}\, \Delta T_r\right)^{3/2} \quad (17)$$

$$\text{Also, we have } \eta_t = P_{load} \big/ (P_{load} + P_t) \quad (18)$$

and

$$\psi_{pd} = P_{load} \big/ V_t \quad (19)$$

In (18) and (19), $P_{\text{load}}$ is the output load of the LHFGT. From (17), it can be concluded that for minimized $P_t$, $V_t$ is also minimum subject to fixed $\Delta T_r$ limit. Since the LHFGT is designed with the $\Delta T_r$ limit being considered as a fixed TDP, therefore, the condition for minimum $P_t$ and $V_t$ holds. This condition can be considered as a Pareto-optimal solution, since, $V_t$ can be further reduced by selecting a smaller core size at the cost of an increase in $\Delta T_r$ and $P_t$. Consequently, the optimality will be lost, since, $P_t$ is no longer minimum and the $\Delta T_r$ limit is no longer satisfied. Hence, $P_t$ may be considered as minimized with minimum-possible $V_t$ subject to the fixed $\Delta T_r$ limit. Now, as per (18) and (19), for minimized $P_t$ and $V_t$, the $\eta_t$ and $\psi_{pd}$ may also be considered as maximized with the same Pareto-optimality. Thus, in a nutshell, the minimization of $P_t$ subject to fixed $\Delta T_r$ limit may be considered as the most critical objective, which leads to the achievement of all the desired Pareto-optimal objectives.

In [42], it is shown that $B_{pk}$ is an essential TDP for LHFGT design optimization, and almost all TDPs depend on it. Therefore, in this paper, to achieve the desired objectives, the $P_t$ is optimized with respect to $B_{pk}$ for optimal LHFGT design, in a similar way as in [42]. The $P_{cu}$, subject to the optimal LSS criteria (15) with HFF $\approx 1$, may be represented using Faraday's law [25] as follows:

$$P_{cu} = \rho_{cu} k_{wu} V_w J_w^2 = \rho_{cu} V_w P_{VA}^2 \Big/ (k_{wu} K_{wf}^2 f_s^2 B_{pk}^2 A_{cr}^2 A_w^2) \quad (20)$$

where $\rho_{cu}$ is electrical conductor-resistivity ($1.72 \times 10^{-8}\Omega$·m), $k_{wu}$ is window utilization factor (value between 0.2-0.5), $P_{VA}$ is total Volt-Ampere power rating, and $K_{wf}$ is the excitation-waveform factor (=0.4 for the square waveform in LLC converters). Also, the $P_{fe}$ may be accurately represented using the waveform-coefficient Steinmetz equation (WcSE) [45], keeping in view the square excitation-waveform of the LHFGT in LLC converters and the core-loss analyses conducted in [34], [45]–[47]. According to [45], the $P_{fe}$ can be represented as,

$$P_{fe} = (\pi/4)\, K_{SE} f_s^{\alpha_{SE}} B_{pk}^{\beta_{SE}} V_{cr} \quad (21)$$

In (21), $\alpha_{SE}$, $\beta_{SE}$, and $K_{SE}$ are the Steinmetz-equation parameters for the core material being used. Now, it can be seen from (20) and (21) that the $P_t$, sum of $P_{cu}$ and $P_{fe}$, depends on $f_s$ and $B_{pk}$. Since, in the LHFGT design for LLC converters, a fixed nominal $f_s$ is considered; therefore, $P_t$ is differentiable with respect to $B_{pk}$, and the point of optima can be obtained. By solving the differential of $P_t$, with respect to $B_{pk}$, equated equal to zero, we get,

$$B_{pk,op} = \left[\frac{8\rho_{cu} V_w [A_{cr} A_w K_w]^{-2}}{\pi \beta_{SE} k_{wu} f_s^{\alpha_{SE}+2} K_{SE} V_{cr} P_{VA}^{-2}}\right]^{1/(\beta_{SE}+2)} \quad (22)$$

Equation (22) is the point of optimality for which the $P_t$ is minimum. Now, (21) is divided by (20) and then combined with (22) to get the following optimality condition,

$$P_{t,opt} = \frac{\beta_{SE}+2}{\beta_{SE}} P_{cu} = \frac{\beta_{SE}+2}{2} P_{fe} \quad (23)$$

Equation (23) is the desired optimality condition that relates the optimal $P_t$ ($P_{t,\text{opt}}$), $P_{cu}$, and $P_{fe}$ through material characteristics. This relationship between the losses holds for LHFGT, only if the optimal LSS criteria (15) is satisfied. In this paper, all the OTDPMs have been formulated, keeping in view this optimality condition (23), for obtaining the desired optimized LHFGT design.

### 2) THE OPTIMAL $B_{PK}$ MODEL (OPFDM)

The $B_{pk}$ is the most important TDP since all other TDPs can be obtained using its value. Equation (22) presents the optimal $B_{pk}$ model for which the $P_t$ is minimized; however, this model, in its current form cannot be used for CWSS, since it is dependent on transformer GFs. Therefore, by using (16), (20) and (21) in (23), and replacing all the GFs with the corresponding ACGFE models, (3) to (9), we get,

$$B_{pk,op} = \left[\left[\frac{1.725^{12} k_{Acr} k_{Aw} k_{MPL} k_{wu} \beta_{SE}}{f_s^{7\alpha_{SE}-2} \rho_{cu} k_w^2 k_{MLT}^{-1} K_{wf}^{-2} K_{SE}^7 P_{VA}^2}\right] \times \left[\frac{h_t k_{srf}\, \Delta T_r}{k_{cr}\, (\beta_{SE}+2)}\right]^8\right]^{\frac{1}{7\beta_{SE}-2}} \quad (24)$$

Equation (24) is the standard form of the proposed OPFDM, based on the optimality condition (23), the ACGFE models (3) to (9), the core material parameters, and the $\Delta T_r$ limit, subject to the square excitation waveform, and the LSS criteria (15). Furthermore, the optimal value of $B_{pk}$, obtained using (24), can be used in obtaining the optimal values of all other TDPs, thus, facilitating the non-iterative optimal design.

### 3) THE OPTIMAL $J_W$ MODEL (OCDM)

The $J_w$ model plays an important role in selecting the $A_{cu-t}$ for the LHFGT windings. Therefore, the $\Delta T_r$ limit, and the optimality criteria (23) need to be considered while formulating its optimal model, the OCDM. By using (23) and (16) in (20), the optimal $J_w$ can be represented as,

$$J_{w,op} = \sqrt{\beta_{SE} h_t A_{srf}\, \Delta T_r \big/ ((\beta_{SE}+2)\rho_{cu} k_{wu} V_w)} \quad (25)$$

The analytical model (25) can be made independent of the GFs by incorporating the ACGFE models (4) and (5) in (25) as follows:

$$J_{w,op} = \left(\sqrt{\beta_{SE} h_t k_{srf}\, \Delta T_r \big/ ((\beta_{SE}+2)\rho_{cu} k_{wu} k_w)}\right) \times A_{prod}^{-\frac{1}{8}} \quad (26)$$

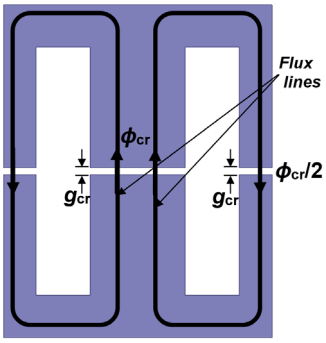


**FIGURE 4.** $g_{cr}$ distribution in the ferrite core of LHFGT, with concentric windings wound on the central limb.

Equation (25) is the proposed OCDM, based on the optimality condition (23), the ACGFE models, the core material parameters, the $A_{\text{prod}}$ value, and the $\Delta T_{\text{r}}$ limit, subject to the optimal LSS criteria (15).

#### 4) THE OPTIMAL $\mu_{\text{E}}$ MODEL (OEPM)

In this paper, the optimal analytical models for the $\mu_{\text{e}}$ (modified $\mu_{\text{r}}$), the $g_{\text{cr}}$ and the $N_{\text{p}}$ are formulated keeping in view the desired $L_{\text{m}}$, the $I_{\text{res}}$, the $I_{\text{mg}}$, and the associated energy storage. These TDPs play an important role in the integration of $L_{\text{m}}$ in the LHFGT primary winding.

In the LHFGT, the $g_{\text{cr}}$ is evenly distributed in all the limbs of the ferrite core to minimize the fringing flux, as shown in Fig. 4. The magneto-motive force (*mmf*) across the magnetic path can be calculated using the magnetic circuital law [23], as follows:

$$\begin{aligned} mmf &= \phi_{cr}\,(l_{cr} + 2\mu_r g_{cr})\big/(\mu_o \mu_r A_{cr}) \\ &= \phi_{cr} l_{cr}\big/(\mu_o \mu_e A_{cr}) \end{aligned} \tag{27}$$

where, $\mu_e = 1\big/\mu_r + 2g_{cr}\big/l_{cr}$

$$\Rightarrow g_{cr} = l_{cr}\,(\mu_r - \mu_e)\big/(2\mu_o \mu_e) \tag{28}$$

Also from the fundamental concepts of magnetics [23], the $L_{\text{m}}$ and $B_{\text{pk,op}}$ can be represented in terms of $N_{\text{p}}$ as follows:

$$L_m = N_p A_{cr} B_{pk,op}\big/I_{mg,pk} \tag{29}$$

and,

$$B_{pk,op} = \mu_o \mu_e N_p I_{mg,pk}\big/l_{cr} \tag{30}$$

In (29) and (30), the $I_{\text{mg,pk}}$ is the peak value of $I_{\text{mg}}$. From (29) and (30) we can get $N_{\text{p}}$ in terms of $L_{\text{m}}$ as,

$$N_p = \sqrt{L_m l_{cr}\big/(\mu_o \mu_e A_{cr})} \tag{31}$$

The optimal values of $N_{\text{p}}$ and $g_{\text{cr}}$ can be obtained based on the desired $L_{\text{m}}$ value, using (28) and (31), if the optimal value of $\mu_{\text{e}}$ ($\mu_{\text{e,op}}$) is known. Therefore, using (29) and (30) to obtain the energy storage with respect to $I_{\text{mg,pk}}$ as,

$$\frac{1}{2} L_m I_{mg,pk}^2 = \frac{1}{2} A_{cr} l_{cr} B_{pk,op}^2 \Big/ (\mu_o \mu_e) \tag{32}$$

Equation (32) presents the energy stored in terms of $B_{\text{pk,op}}$. Furthermore, the stored energy can also be represented in terms of peak-$I_{\text{res}}$ ($I_{\text{res,pk}}$) and $J_{\text{w,op}}$. Since, the $I_{\text{res}}$ is the input current to the LHFGT, therefore, it can be represented as,

$$I_{res} = J_{w,op} A_{cu,p} = J_{w,op} x_{wu,p} k_{wu} A_w \big/ N_p \tag{33}$$

In (33), $A_{\text{cu,p}}$ is the $A_{\text{cu}-\text{t}}$ for the primary winding, and $x_{\text{wu,p}}$ defines the portion of the total available winding window-area ($k_{\text{wu}} \cdot A_{\text{w}}$) allocated to the primary winding. For the LHFGT having one primary and two secondary windings, with turns-ratio of the form a:1:1, the value for $x_{\text{wu,p}}$ can be obtained using the concept of winding window-area allocation with minimized DC loss [23] as follows:

$$x_{wu,p} = aI_{res}\big/(aI_{res} + 2I_{\text{sec}});\; x_{wu,s} = I_{\text{sec}}\big/(aI_{res} + 2I_{\text{sec}}) \tag{34}$$

In (34), $I_{\text{sec}}$ is the rms current in each of the secondary windings, and $x_{\text{wu,s}}$ is the portion of the total available winding window-area allocated to each of the secondary windings. Also, $x_{\text{wu,p}} + 2 \cdot x_{\text{wu,s}} = 1$. Therefore, the stored energy in terms of $I_{\text{res,pk}}$ and $J_{\text{w,op}}$ can be represented using (31) and (33) as,

$$\begin{aligned} \frac{1}{2} L_m I_{res,pk}^2 &= L_m I_{res}^2 \Big/ \left(2K_i^2\right) \\ &= \mu_o \mu_e A_{cr} x_{wu,p}^2 k_{wu}^2 A_w^2 J_{w,op}^2 \Big/ \left(2K_i^2 l_{cr}\right) \end{aligned} \tag{35}$$

where, $K_i = I_{res}\big/I_{res,pk}$

By dividing (35) with (32), we get,

$$\mu_{e,op} = B_{pk,op} l_{cr} I_{res} \big/ \left(\mu_o x_{wu,p} k_{wu} A_w J_{w,op} I_{mg,pk}\right) \tag{36}$$

By using the ACGFE models (7) and (8) in (36), we get,

$$\mu_{e,op} = B_{pk,op} k_{MPL} I_{res} \Big/ \left(\mu_o x_{wu,p} k_{wu} k_{Aw} J_{w,op} I_{mg,pk} A_{prod}^{1/4}\right) \tag{37}$$

Equation (37) is the desired analytical OEPM, in terms of $B_{\text{pk,op}}$, $J_{\text{w,op}}$, $I_{\text{res}}$, $I_{\text{mg,pk}}$, $A_{\text{prod}}$, and the ACGFE parameters. Using this proposed model, the optimal values of $N_{\text{p}}$ and $g_{\text{cr}}$ can be obtained (from (28) and (31)) for integration of the desired $L_{\text{m}}$ in the LHFGT, respectively.

### D. THE OPTIMAL $A_{prod}$ MODEL (OAPM)

In transformer design, the core size is selected based on the $A_{\text{prod}}$ value, which is the product of the $A_{\text{cr}}$ and the $A_{\text{w}}$ of the LHFGT. The desired OAPM, for integrating the $L_{\text{m}}$ while keeping the thermal constraints within limits, can also be obtained from the energy equations (32) and (35). By multiplying (32) and (35), we get,

$$L_m^2 I_{mg,pk}^2 I_{res}^2 = A_w^2 A_{cr}^2 B_{pk,op}^2 x_{wu,p}^2 k_{wu}^2 J_{w,op}^2 \tag{38}$$

By using (26) in (38), and simplifying, we get the optimal $A_{\text{prod}}$ as,

$$A_{prod,op} = \left[\frac{K_{prod}}{\Delta T_r}\left(\frac{L_m I_{mg,pk} I_{res}}{B_{pk,op}}\right)^2\right]^{\frac{4}{7}} \tag{39}$$

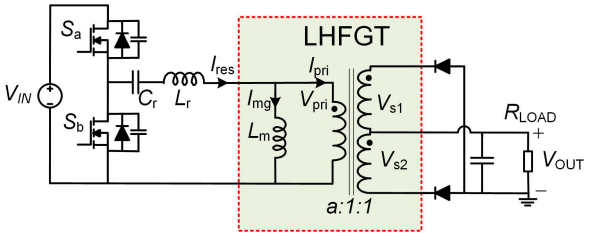


**FIGURE 5.** The LLC converter configuration. ($V_{IN}$: Input voltage, $S_a$ and $S_b$: MOSFET switches, $C_r$: resonant capacitor, $L_r$: resonant inductor, $I_{pri}$: primary current, $V_{pri}$: primary voltage, $V_{s1}$ and $V_{s2}$: secondary voltages, $a$: turns ratio, $V_{OUT}$: output voltage, $R_{LOAD}$: load resistor.)

where, $K_{prod} = \rho_{cu} k_w (\beta_{SE} + 2) \Big/ \left(\beta_{SE} h_t k_{srf} x_{wu,p}^2 k_{wu}\right)$

Equation (39) is the desired proposed OAPM for CWSS of LHFGT in LLC converters, based on the LLC circuit parameters, the optimality condition (23), the core material parameters, the ACGFE models, the $\Delta T_r$ limit, the OPFDM, and the optimal LSS criteria (15). Similarly, for ease in design, the OCDM (26) and the OEPM (37) can also be represented in terms of the newly defined constant $K_{prod}$ as follows:

$$J_{w,op} = \left[\Delta T_r \Big/ \left(K_{prod} x_{wu,p}^2 k_{wu}^2\right)\right]^{\frac{1}{2}} \times A_{prod}^{-1/8} \quad (40)$$

and,

$$\mu_{e,op} = \left[K_{prod}^{-1/2} B_{pk,op} k_{MPL} I_{res} \Big/ \left(\mu_o k_{Aw} I_{mg,pk} \Delta T_r^{1/2}\right)\right] \times A_{prod}^{-1/8} \quad (41)$$

### E. THE WINDING SELECTION

The winding selection for LHFGT in LLC converters comprises of the following steps:

Step-1: Litz-wire $r_s$ selection based on the optimal LSS model (15).

Step-2: Optimal $N_p$ calculation, using (31) with $\mu_{e,op}$ calculated using (41), followed by the calculation of the turns of both secondary windings ($N_{s1} = N_{s2} = N_p/a$).

Step-3: Litz-wire $S_t$ calculation for primary ($S_p$) and secondary ($S_{s1}$ and $S_{s2}$) windings, as follows:

$$S_p = I_{res} \Big/ \left(\pi r_s^2 J_{w,op}\right)$$
$$S_{s1} = S_{s2} = I_{sec} \Big/ \left(\pi r_s^2 J_{w,op}\right) \quad (42)$$

Step-4: Arranging the windings concentrically around the selected ferrite core's central-limb, with full-interleaving.

It may be noted that the same value of $J_{w,op}$ is used for both the primary and secondary windings in (42) to have a uniform distribution of heat across the winding surface. Also, fully interleaved winding arrangement is selected keeping in view the optimization aim.

## III. THE PROPOSED ANALYTICAL DESIGN-METHOD AND ITS VERIFICATION

### A. THE PROPOSED DESIGN METHODOLOGY

In this paper, the basic LLC converter topology that has been taken as an example to show the implementation of the proposed method for the LHFGT design is shown in Fig. 5. In this topology, the primary side of the LHFGT comprises of the half-bridge LLC resonant tank, whereas the secondary side consists of the center-tapped synchronous-rectifier. The main specifications of the converter, taken as input in the proposed LHFGT design methodology, have been presented in Table 2. Based on these input application requirements, the core and winding size are selected using the analytical models proposed in Section-II, i.e., the proposed OTDPMs and the proposed OAPM. The complete proposed design process, i.e., the non-iterative optimal design methodology of the LHFGT, has been presented in Fig. 6.

**TABLE 2.** Main specifications of the LLC converter (design process input).

| Parameter | Value | Parameter | Value |
|---|---|---|---|
| $V_{IN}$ | 360V (nom.)<br>400V (max.) | Load power ($P_{load}$) | 200W |
| $V_{OUT}$ | 12V | $a$ | 14 |
| $\Delta T_r$ | 50°C | $f_s$ | 110kHz |
| $I_{res}$ | 2.5053A | $L_m$ | 128µH |
| $I_{mg,pk}$ | 3.2326A | $C_r$ | 0.066µF |
| $I_{sec}$ | 13.5417A | $L_r$ | 37.25µH |

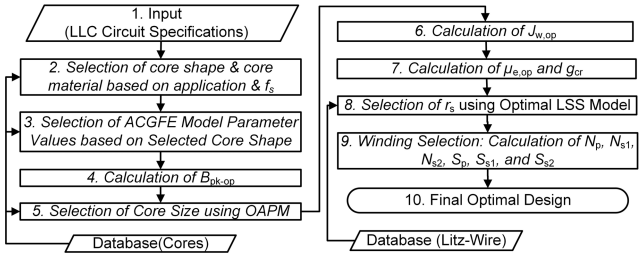


**FIGURE 6.** The proposed design process for LHFGT in LLC converters.

In this proposed method, the designer is required to select the core shape and the core material keeping in view the application requirements, the optimization aim, and the $f_s$. The characteristic curves (loss density curves) provided in the datasheet for various core-shapes and core-materials can be used for this selection. The designer may select more than one core-shape or core-material for LHFGT design; however, in this case, the number of iterations ($N_{iterations}$) will be based on the number of selected shapes and materials, that is,

$$N_{iterations} = N_{core-shape} \times N_{core-material} \quad (43)$$

where, $N_{core-shape}$ is the number of the selected ferrite core-shapes, and $N_{core-material}$ is the number of selected core-materials. For each selected core shape and material, the proposed method gives an optimal design. In the end, the combination that provides the best results can be selected for the final design implementation. This shows that the criteria for the proposed method to be non-iterative requires the selection of core-shape and core-material in start of the process. However, even if the designer selects multiple core shapes and materials, the maximum number of iterations as a result of these discrete choices is still very small as compared to the iterations in the existing multi-objective optimization techniques [7], [9], [13]–[20]; hence, the proposed process remains time and resource-efficient, with easy implemen-

**TABLE 3.** Main specifications of the ferrite core-materials.

| Parameter | N72 | PC40 |
|---|---|---|
| $K_{SE}$ | 1.076 | 1.064 |
| $\alpha_{SE}$ | 1.558 | 1.401 |
| $\beta_{SE}$ | 3.114 | 2.185 |
| $\mu_r$ | 2500 | 2300 |
| Saturation flux-density ($B_{sat}$) | 0.4T | 0.5T |
| Density ($\rho_m$) | 4750kg/m$^3$ | 4800kg/m$^3$ |

tation. The designers can also use this method to compare different core shapes and materials for an even more, better design.

### B. RESULTS AND VERIFICATION

In this sub-section, the accuracy and the optimality of the proposed method are verified through comparison with the benchmark method [11], the brute-force iterative optimization, the genetic algorithm (GA)-based optimization [7], as well as, the FEM simulations. In order to perform the analytical comparison, the LHFGT losses are calculated using (11), (16), (20), and (21), the $\eta_t$ is calculated using (18), and the $\psi_{pd}$ is calculated using (19). The $P_t$ & $V_t$ product ($P_t \cdot V_t$) is used for evaluating the optimality of the designs. Other objectives, such as the $\psi_{pd}$ and the $\eta_t$ are also analyzed. Furthermore, the $\Delta T_r$ is calculated using the following model [24],

$$\Delta T_r = 450 \times \left[P_t / A_{srf} \times 10^{-4}\right]^{0.826} \tag{44}$$

#### 1) COMPARISON WITH THE BENCHMARK METHOD

In order to verify the accuracy, the proposed CWSS method is compared with the existing benchmark method [11], using two different ferrite core materials (PC40 and N72, with material specifications shown in Table 3). In this comparison, both methods have the same input values (Table 2). Since an assumption is made for the $B_{pk}$ value in [11]; therefore, the value obtained using the proposed $B_{pk}$ model (24) of this paper, and the proposed $B_{pk}$ model of [42], are used as an input to the benchmark method [11]. The comparison results in this regard have been shown in Table 4. In the tabulated results, the percentage differences in $P_t \cdot V_t$ values ($P{\cdot}V$ %Diff.), $\eta_t$ values ($\eta_t$ %Diff.), and $\psi_{pd}$ values ($\psi_{pd}$ %Diff.), with reference to the proposed design, are also shown as a means of assessing accuracy improvement.

The results show a percentage improvement of 13% to 48% in the $\psi_{pd}$ maximization, and 21% to 57% in the $P_t \cdot V_t$ minimization of the LHFGT designed using the proposed method in comparison to the benchmark [11] and [42] for both type of materials, respectively. A small improvement can also be seen in $\eta_t$ values (0.03% to 0.22%). This verifies the accuracy improvement in using the proposed OTDPMs and the OAPM for LHFGT design in LLC resonant converters.

#### 2) COMPARISON WITH THE BRUTE-FORCE ITERATIVE OPTIMIZATION

In order to verify the optimality, the optimal design obtained using the proposed CWSS method is compared with that

**TABLE 4.** Proposed method design vs the benchmark [11] and [42].

| Parameter | N72 material based designs | | | PC40 material based designs | | |
|---|---|---|---|---|---|---|
| | $T_{1\text{-N72}}$ Proposed | $T_{2\text{-N72}}$ [11] | $T_{3\text{-N72}}$ [11]+[42] | $T_{1\text{-PC40}}$ Proposed | $T_{2\text{-PC40}}$ [11] | $T_{3\text{-PC40}}$ [11]+[42] |
| **Design** | | | | | | |
| $B_{pk}$ (T) | 0.1447 | 0.1447 | 0.1417 | 0.1622 | 0.1622 | 0.1572 |
| Core size | EER28 | EER35 | EER28L | EER28 | EER28L | EER28 |
| $g_{cr}$ (mm) | 0.567 | 0.446 | 0.450 | 0.465 | 0.290 | 0.265 |
| $r_s$ (mm) | 0.05 | 0.20 | 0.20 | 0.05 | 0.20 | 0.20 |
| $N_p$:$N_{s1}$:$N_{s2}$ | 38:3:3 | 30:2:2 | 34:2:2 | 34:2:2 | 28:2:2 | 26:2:2 |
| $S_p$, $S_{s1}$ | 47, 256 | 8, 42 | 6, 31 | 51, 277 | 8, 42 | 7, 38 |
| **Results** | | | | | | |
| $V_t$ (cm$^3$) | 6.799 | 13.151 | 8.481 | 6.602 | 8.900 | 7.627 |
| $P_{cu}$ (W) | 1.362 | 1.136 | 1.346 | 0.984 | 1.063 | 1.235 |
| $P_{fe}$ (W) | 0.799 | 1.468 | 0.872 | 0.987 | 1.149 | 0.922 |
| $P_t$ (W) | 2.161 | 2.604 | 2.218 | 1.971 | 2.213 | 2.157 |
| $\Delta T_r$ (°C) | 43.690 | 33.077 | 39.575 | 40.48 | 39.50 | 43.61 |
| $\eta_t$ (%) | 98.93% | 98.71% | 98.90% | 99.02% | 98.91% | 98.93% |
| **$\eta_t$ %Diff.** | **0.0%** | **0.22%** | **0.03%** | **0.0%** | **0.11%** | **0.09%** |
| $\psi_{pd}$ (W/cm$^3$) | 29.418 | 15.208 | 23.583 | 30.294 | 22.472 | 26.224 |
| **$\psi_{pd}$ %Diff.** | **0%** | **48%** | **20%** | **0%** | **26%** | **13%** |
| $P_t{\cdot}V_t$ (W·cm$^3$) | 14.694 | 34.250 | 18.808 | 13.010 | 19.691 | 16.447 |
| **$P{\cdot}V$ %Diff.** | **0%** | **57%** | **22%** | **0%** | **34%** | **21%** |

obtained using an iterative brute-force optimization procedure. The input data from Table 2 is used for designing the LHFGTs in this comparison. The PC40 core material and the EER-shaped core is selected for the comparison, based on the application requirements. In the brute-force method, the optimal solution is obtained by searching the optimal values of the independent TDPs or the OVs within a pre-specified range, while the CWSS method remains the same. Therefore, the proposed CWSS models of this paper are used in the brute-force optimality search. Since, in the proposed method, all TDP models are directly or indirectly dependent on the $B_{pk}$ value, therefore, in the brute-force iterative search, only the $B_{pk}$ value is varied from a minimum value of 0.05T to a maximum value of 0.3T (less than the $B_{sat}$) for optimality search. In each iteration, the value of $B_{pk}$ is changed using a very small step size; however, for reducing the number of total iterations, initially a larger step size is considered, and then gradually the step size is reduced until the solutions converge. In the initial phase (phase-1), the iterations are performed with a step size of 0.05T. At the end of the initial iteration-phase, two most optimal solutions (MOSs) are selected. In the next iteration-phase, the iterations are repeated using a reduced step size between the $B_{pk}$ values of the two MOSs from the previous iteration-phase. The process is repeated until convergence is achieved, that is, the MOS of the current iteration-phase matches with the MOS of the previous iteration-phase. In the end, this optimal solution is compared with the optimal solution obtained using the proposed methodology. The results of the comparison have been furnished in Table 5 and Fig. 7, respectively. In the results, P1#1 & P2#2 represent the MOSs of phase-1, P2#1 & P2#2 represent the MOSs of phase-2, and P3#1 & P3#2 represent the MOSs of phase-3. Since the design $T_4$ is the MOS for phase 2 (P2#1) and phase 3 (P3#1), hence, it is

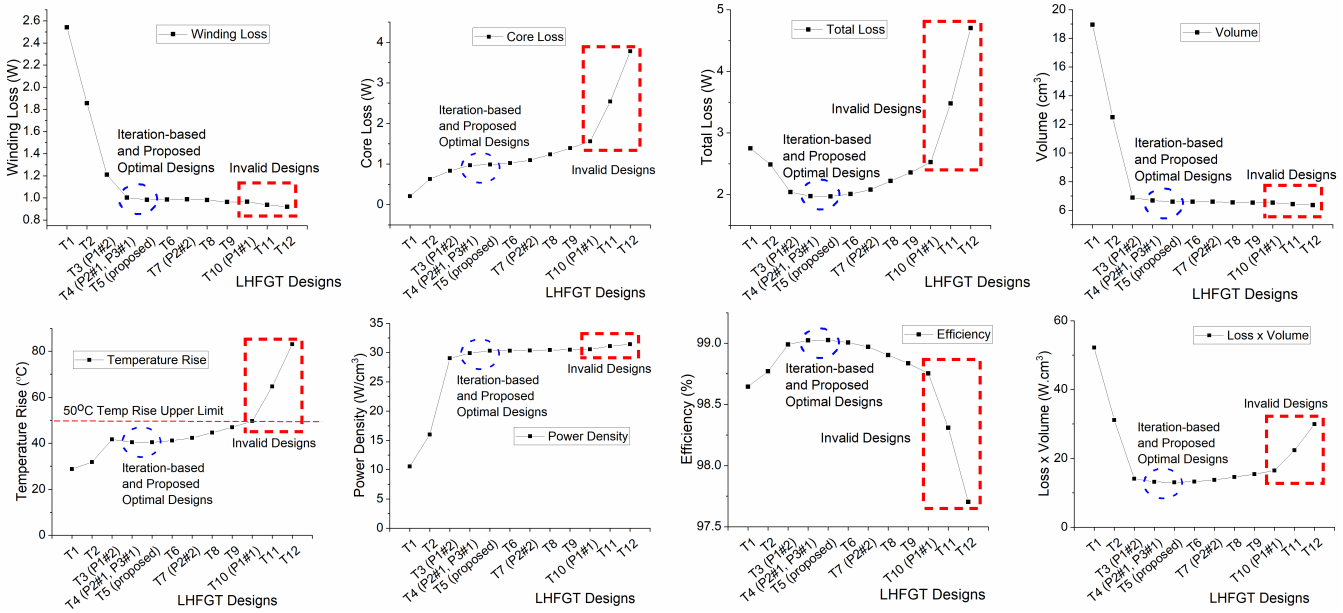


**FIGURE 7.** The LHFGT design results for the optimality verification. The designs inside red square region are invalid due to violation of the temperature-rise limit. The blue encircled designs include the iterations-based optimal design ($T_4$) and the proposed method-based optimal design ($T_5$ ).

**TABLE 5.** The LHFGT designs for the optimality verification.

| Phase & Step Size | LHFGT Design | Parameters | | | | | |
|---|---|---|---|---|---|---|---|
| | | $B_{pk}$ (T) | $A_{prod}$ (cm$^4$) | EER Core Size | $g_{cr}$ (mm) | $N_p$:$N_{s1}$ :$N_{s2}$ | $S_p$, $S_{s1}$ |
| Phase-1 (0.05T) | $T_1$ | 0.05 | 3.128 | 40 | 2.929 | 64:5:5 | 60,323 |
| | $T_2$ | 0.10 | 1.417 | 35 | 1.372 | 51:4:4 | 55,298 |
| | $T_3$ (P1#2) | 0.15 | 0.891 | 28 | 0.496 | 36:3:3 | 52,281 |
| Phase-2 (0.01T) | **$T_4$ (P2#1, P3#1)** | **0.16** | **0.828** | **28** | **0.470** | **35:2:2** | **51,277** |
| | **$T_5$(proposed)** | **0.1622** | **0.815** | **28** | **0.465** | **34:2:2** | **51,277** |
| Phase-3 (0.005T) | $T_6$ (P3#2) | 0.165 | 0.799 | 28 | 0.458 | 34:2:2 | 51,276 |
| Phase-2 (0.01T) | $T_7$ (P2#2) | 0.17 | 0.773 | 28 | 0.447 | 34:2:2 | 51,274 |
| | $T_8$ | 0.18 | 0.724 | 28 | 0.425 | 33:2:2 | 50,272 |
| | $T_9$ | 0.19 | 0.680 | 28 | 0.405 | 32:2:2 | 50,270 |
| Phase-1 (0.05T) | $T_{10}$ (P1#1) | 0.20 | 0.642 | 28 | 0.387 | 32:2:2 | 50,268 |
| | $T_{11}$ | 0.25 | 0.479 | 28 | 0.317 | 29:2:2 | 48,260 |
| | $T_{12}$ | 0.30 | 0.404 | 28 | 0.271 | 27:2:2 | 47,252 |

the converged optimal design obtained as a result of the iterative optimization process. The design $T_5$ is the optimal design obtained using the proposed method that has also been shown in the results, adjacent to the iteration-based optimal design $T_4$, for comparison.

The results show that the iteration-based optimal design $T_4$ matches with the proposed method-based optimal design $T_5$ with a minimal error difference (1.3% in the $\psi_{pd}$, and 1.4% in the $P_t \cdot V_t$). The results verify that the proposed OAPM-based design methodology results in the optimal design of the LHFGT in a single iteration. Furthermore, the importance and optimality of the proposed $B_{pk}$ model (24) are also verified through comparison with the value of $B_{pk}$ for which the iterative brute-force optimization process has converged to optimality (error 1.38%).

### 3) COMPARISON WITH THE GA-BASED OPTIMIZATION

In this sub-section, the optimality and the utility of the proposed method are verified through comparison with the GA-based iterative optimization [7]. The proposed OAPM-based method is implemented in designing the LHFGT for the LLC converter application presented in [7]. The obtained results are then compared with the results in [7], as shown in Table 6. In the table, $d_s$ is the inter-winding space, required for integration of the $L_r$, that can be calculated using the following equation [7]:

$$d_s = \frac{1}{M_s}\left(\frac{L_r b_l}{\mu_o l_w}\left(\frac{M_s}{N_p}\right)^2 - \frac{2r_s n_l}{3}\right) \tag{45}$$

In (45), $M_s$ is the number of magnetic sections, and $n_l$ is the total number of primary and secondary layers. The results in Table 6 show that the proposed OAPM-based design method results in the optimal LHFGT design in a single iteration as compared to the 40,000 iterations of the GA-based method [7]; this verifies the utility and the optimality of the proposed method.

### 4) COMPARISON WITH THE FEM SIMULATION

FEM simulations in the software ANSYS Maxwell have been carried out to ensure that the $B_{pk}$ values, inside the cores of the designed LHFGTs, match with those obtained using the proposed optimal $B_{pk}$ model (24). The 3D FEM models of the proposed method based designs presented in Table 4, i.e., $T_{1-N72}$ and $T_{1-PC40}$, have been built for this verification. The flux density plots obtained as a result of the simulations have been shown in Fig. 8. The simulation results show that the $B_{pk}$

**TABLE 6. Proposed method design vs the GA-based optimal design [7].**

| Parameter | GA [7] | Proposed | Parameter | GA [7] | Proposed |
|---|---|---|---|---|---|
| $B_{pk}$ (T) | 0.23 | 0.2954 | $L_m$ ($\mu$H) | 1980 | 2000 |
| $d_s$ (mm) | 1.5 | 4.9984 | $L_t$ ($\mu$H) | 31 | 30 |
| $g_{cr}$ (mm) | 0.63 | 0.4265 | $V_t$ (dm$^3$) | 0.74 | 0.44 |
| $M_s$ | 1 | 2 | $\Delta T_r$ (°C) | 59.98 | 54.597 |
| Core size | EE100/60 | E100/60 | $\eta_t$ (%) | 99.43 | 99.67 |
| $r_s$ (mm) | 0.1 | 0.115 | $P_t$ (W) | 68.6 | 39.7686 |
| $S_p$ | 150 | 61 | $P_t \cdot V_t$ | 50.76 | 17.43 |
| $S_s$ | 150 | 61 | (W·dm$^3$) | | |
| $N_p$:$N_s$ | 40:40 | 46:46 | $N_{iterations}$ | 40,000 | 1 |

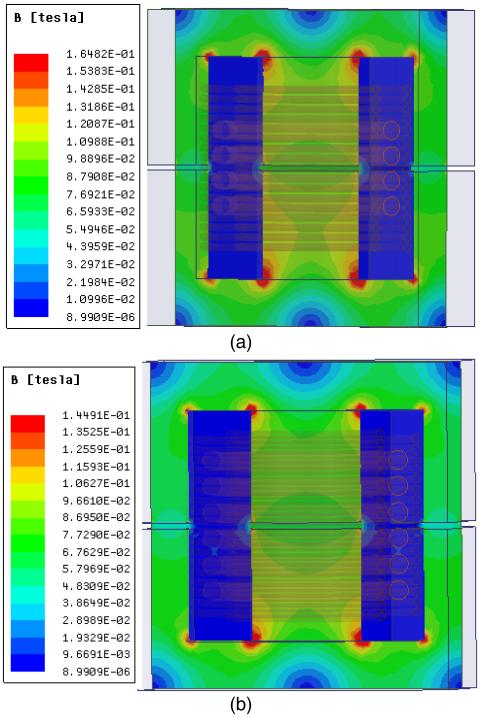


**FIGURE 8. FEM Simulation results showing flux density plot inside the LHFGT core. (a) PC40 based $T_{1-PC40}$ design with $B_{pk} = 0.1648$T. (b) N72 based $T_{1-N72}$ design with $B_{pk} = 0.1449$T.**

values obtained from these plots match the values obtained using the proposed $B_{pk}$ model (24) with a minimal error of 1.6% and 0.14% in case of $T_{1-N72}$ and $T_{1-PC40}$ designs, respectively. Hence, the accuracy of the designed LHFGTs is verified.

## IV. EXPERIMENT RESULTS

In this section, the proposed OAPM-based non-iterative analytical design methodology for LHFGT in LLC converters is validated through experimental testing of a prototype transformer built as per the $T_{1-PC40}$ design specifications shown in Table 4. The prototype LHFGT is shown in Fig. 9 (a), respectively.

### A. $P_{FE}$ AND $P_{CU}$ LOSSES MEASUREMENT TESTING

The $P_{fe}$ and $P_{cu}$ loss measurement testing is performed for the validation of the $P_t$, $\eta_t$, $\psi_{pd}$, and $P_t \cdot V_t$ analytical results shown in Table 4 for the $T_{1-PC40}$ design. The tests have been performed as per the methods proposed in [48] for $P_{fe}$ measurement and in [49] for $P_{cu}$ measurement.

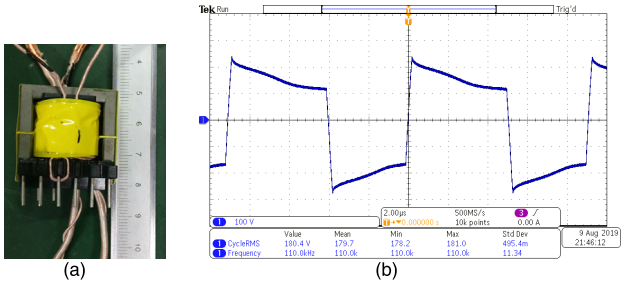


**FIGURE 9. (a) 200W $T_{1-PC40}$ prototype LHFGT for experimental testing. (b) Power amplifier output waveform.**

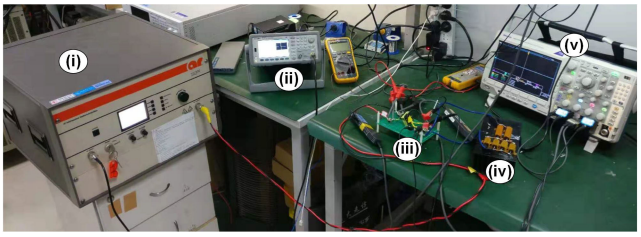


**FIGURE 10. $P_{fe}$ and $P_{cu}$ loss measurement setup. (i) AR power amplifier. (ii) Agilent signal generator. (iii) Device under test (DUT). (iv) 200W resistive load used in $P_{cu}$ loss measurement test only. (v) Oscilloscope.**

**TABLE 7. $P_{cu}$ and $P_{fe}$ measurement test results.**

| Parameter | Experimental | Analytical | %error |
|---|---|---|---|
| $P_{cu}$ (W) | 1.025 | 0.984 | 4.17% |
| $P_{fe}$ (W) | 1.006 | 0.987 | 1.93% |
| $P_t$ (W) | 2.031 | 1.971 | 3.04% |
| $P_t \cdot V_t$ (W·cm$^3$) | 13.41 | 13.010 | 3.06% |
| $\psi_{pd}$ (W/cm$^3$) | 30.294 | 30.294 | 0.00% |
| $\eta_t$ (%) | 98.99% | 99.02% | 0.03% |

The experimental platform for these tests has been shown in Fig. 10. In these tests, the waveform signal generator (Agilent 33521A) and the RF power amplifier (AR 500A250B) have been used for providing the square excitation voltage waveform for carrying out the tests. The waveform has been shown in Fig. 9(b). This waveform is not a perfect square waveform due to the power amplifier with a pure inductance load (the transformer) connected directly at its output. However, care has been taken, and the input voltage RMS value has been maintained at 180V, which is the RMS value of the primary voltage of the LHFGT in the LLC converter (Table 2). Furthermore, this waveform distortion does not affect the measurement results, since, the method considers this nonlinearity in the measurement process and takes the average value of the $P_{fe}$ and $P_{cu}$ losses over one waveform cycle.

The experiment results have been presented in Table 7, where the analytical results from Table 4 have also been shown for comparison purpose. The comparison results show that the experimental results agree with the analytical results with a marginal error of less than 5% in all parameters. These results, therefore, validate the accuracy of the loss models (11), (16), (20), and (21), and the analytical results of Section III for optimality and accuracy verification of the proposed methodology. Furthermore, these results can also be used for validation of the optimality condition (23).

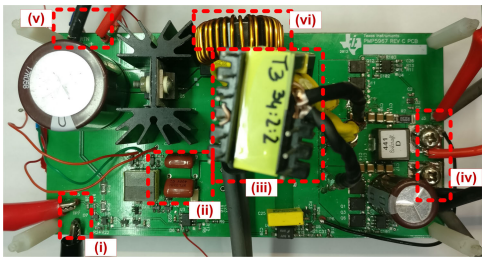


**FIGURE 11.** PMP5967 LLC converter board and the prototype LHFGT. (i) 12V Bias. (ii) $C_r$. (iii) The prototype LHFGT (DUT). (iv) 12V DC output. (v) 360V – 400V DC input. (vi) $L_r$.

By using the loss data of Table 7, and the core material data of Table 3 in (23), we get,

$$P_{t,check} = \frac{\beta_{SE}+2}{\beta_{SE}} P_{cu} = \frac{4.185}{2.185} \times 1.025 = 1.963 \cong 2.031 = P_{t,\exp} \quad (46)$$

$$P_{t,check} = \frac{\beta_{SE}+2}{2} P_{fe} = \frac{4.185}{2} \times 1.006 = 2.105 \cong 2.031 = P_{t,\exp} \quad (47)$$

The resulting $P_{\text{t,check}}$ values in (46) and (47) match with the experimental value ($P_{\text{t,exp}}$) with an error of less than 5%. This validates the optimality of the proposed OAPM design methodology in addition to its accuracy.

### B. PERFORMANCE VALIDATION THROUGH TESTING OF THE PROTOTYPE IN LLC CONVERTER

In this sub-section, the experimental results of the prototype LHFGT by connecting it in an LLC converter test board are presented. The Texas Instruments test board PMP5967 [50] with specifications as mentioned in Table 2 and topology as shown in Fig. 5 is used. The test board, along with the connected LHFGT prototype, is shown in Fig. 11. Before connecting the prototype LHFGT with the LLC test board, the $L_{\text{m}}$ of the prototype has been verified through measurement using the precision LCR meter (Agilent 4285A) with a measured value of 128.1 $\mu$H, accurately matching with the design value. The complete test platform for testing the prototype LHFGT in the LLC converter board has been shown in Fig. 12.

The current and voltage waveforms, showing zero-voltage switching (ZVS), have been recorded for the input of 360VDC, 380VDC, and 400VDC, respectively, and shown in Fig. 13. The voltage across the MOSFET becomes zero ($V_{\text{DS}} = 0$V) due to the resonant circuit well before the MOSFET turns-on ($V_{\text{GS}} > 3$V). Furthermore, all the waveforms (in Fig. 13) are in compliance with the specifications in [50]. The efficiency results of the converter under the input voltages of 360VDC, 380VDC, and 400VDC with varying load have been presented in Fig. 14. These efficiency results have also been compared with the results of the benchmark [11], and the OEM [50], in the same figure for comparison. The efficiency results have been obtained using input and output current and voltage measurements, recorded using high-precision multimeters (Agilent 34410A),

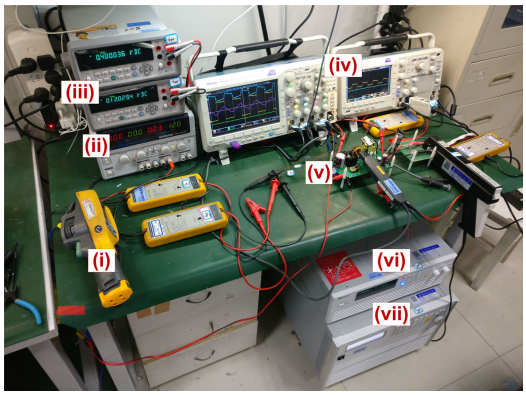


**FIGURE 12.** Experimental platform for testing the prototype LHFGT in the LLC converter. (i) Thermal imager (Fluke Ti200). (ii) 12V bias supply. (iii) Precision digital multimeters (Agilent 34410A). (iv) Oscilloscopes (Tektronix). (v) The LLC converter board along with the prototype LHFGT (DUT). (vi) 360V – 400V DC input power supply (Chroma 62150H-600S). (vii) Electronic DC variable load (Chroma 63804).

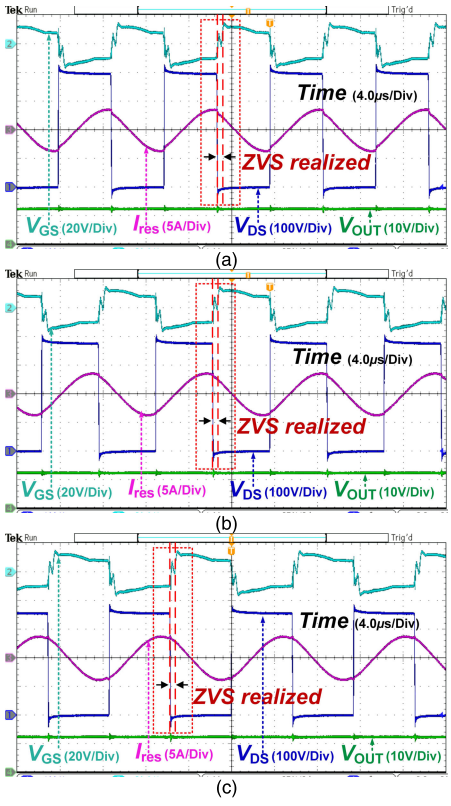


**FIGURE 13.** LLC resonant circuit waveforms depicting ZVS. Here, primary-side MOSFET $S_a$ voltages: drain-source ($V_{DS}$), gate-source ($V_{GS}$ ). (a) 400V DC input. (b) 380V DC input. (c) 360V DC input.

and the high-precision in-built measuring circuits of the DC power supply (Chroma 62150H-600S) and the DC electronic load (Chroma 63804), all having a high measurement accuracy of ±0.1%. The output voltage of the converter with varying load has also been shown in Fig. 14, respectively. Furthermore, the maximum $\Delta T_{\text{r}}$ value, after approximately 35 minutes of continuous operation under 200W load with natural convection, has also been recorded using the thermal imager (Fluke Ti200) and shown in Fig. 15. This $\Delta T_{\text{r}}$

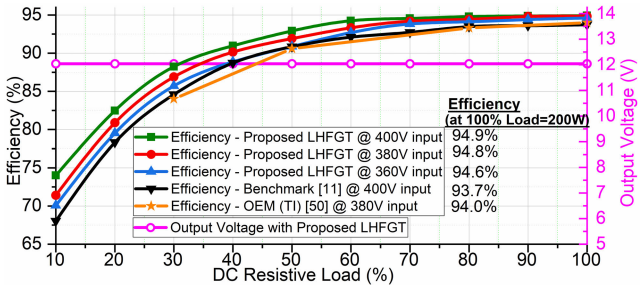


**FIGURE 14.** LLC converter efficiency and output voltage results at various input voltages and load values.

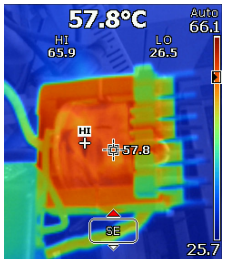


**FIGURE 15.** Thermal image of the prototype LHFGT using Fluke Ti200 after 35 minutes of continuous operation under 200W load with natural convection with $\Delta T_r = 40.4°C$.

value (40.4°C) obtained experimentally matches the analytically obtained value (40.48°C, Table 4) using the thermal model (44), thereby, validating the accuracy of the thermal model (44) and the $\Delta T_r$ results of Section III. The results presented in Figs. 13, 14, and 15 validate the performance of the prototype LHFGT, enabling ZVS operation with better efficiency in comparison to [11] and [50].

The experimental results, presented in Sections IV(A) and IV(B), validate the accuracy and optimality of the results presented in Section III, and the analytical models proposed in Section II. Therefore, it is concluded that the prototype LHFGT demonstrates the desired objectives of this paper, i.e., maximized $\eta_t$ and $\psi_{pd}$, minimized $P_t$ and $V_t$, integrated $L_m$, and maintained $\Delta T_r$ within limits.

## V. CONCLUSION

This manuscript presents an OAPM-based non-iterative analytical design methodology for LHFGT in LLC converters, with maximized $\eta_t$ and $\psi_{pd}$, minimized $P_t$ and $V_t$, integrated $L_m$, and maintained $\Delta T_r$ within limits. The proposed models for the TDPs and the OAPM, used in CWSS process, are formulated keeping in view the interdependency between the TDPs, and by incorporating the LLC circuit parameters, the optimal LSS model, the core material parameters, the proposed ACGFE models, the square excitation-waveform shape in LLC converters, the stored energy due to $g_{cr}$, and the overall optimization aim. The proposed methodology is a simple, less resource-consuming, and time-efficient analytical CWSS approach, that has addressed the limitations of the existing design methods. The analytical and experimental results presented in Sections III and IV, using a 200W LHFGT prototype for the 110kHz 400V-12V dc-dc LLC converter, have validated the accuracy and the optimality of the proposed non-iterative design methodology, ensuring its utility for the converter designers. The proposed OAPM-based design method has shown better results with accuracy in comparison to the methods in [11], and [42]; a percentage improvement of up to 48% in the $\psi_{pd}$ maximization and 57% in the $P_t \cdot V_t$ minimization is achieved. The proposed method has also provided optimal results in a single iteration in comparison to the forty-thousand iterations of GA in [7], demonstrating the efficiency and utility in LHFGT design. The improvement of up to 1.2% in converter efficiency in comparison to the benchmark method [11] ensures the accuracy and optimality of the proposed methodology.

In addition to the LLC resonant converters application, the proposed OAPM-based method can also be used for designing the LHFGT in other types of resonant converters that have a non-sinusoidal square voltage excitation waveform and require $L_m$ integration, such as DAB or CLLC converters.

## REFERENCES

[1] Y. Shen, W. Zhao, Z. Chen, and C. Cai, "Full-bridge LLC resonant converter with series-parallel connected transformers for electric vehicle on-board charger," *IEEE Access*, vol. 6, pp. 13490–13500, 2018.
[2] M. Mu and F. Lee, "Design and optimization of a 380–12 V high-frequency, high-current LLC converter with GaN devices and planar matrix transformers," *IEEE J. Emerg. Sel. Topics Power Electron.*, vol. 4, no. 3, pp. 854–862, Sep. 2016.
[3] N. Salehi, H. Martinez-Garcia, and G. Velasco-Quesada, "A comparative study of different optimization methods for resonance half-bridge converter," *Electronics*, vol. 7, no. 12, p. 368, Dec. 2018.
[4] Z. Zhao, Q. Xu, Y. Dai, and H. Yin, "Analysis, design, and implementation of improved LLC resonant transformer for efficiency enhancement," *Energies*, vol. 11, no. 12, p. 3288, Nov. 2018.
[5] G. K. Y. Ho, Y. Fang, and B. M. H. Pong, "A multiphysics design and optimization method for air-core planar transformers in high-frequency LLC resonant converters," *IEEE Trans. Ind. Electron.*, vol. 67, no. 2, pp. 1605–1614, Feb. 2020.
[6] S. Li, Q. Min, E. Rong, R. Zhang, X. Du, and S. Lu, "A magnetic integration half-turn planar transformer and its analysis for LLC resonant DC-DC converters," *IEEE Access*, vol. 7, pp. 128408–128418, 2019.
[7] A. Garcia-Bediaga, I. Villar, A. Rujas, L. Mir, and A. Rufer, "Multiobjective optimization of medium-frequency transformers for isolated soft-switching converters using a genetic algorithm," *IEEE Trans. Power Electron.*, vol. 32, no. 4, pp. 2995–3006, Apr. 2017.
[8] S. Guo, P. Liu, L. Zhang, and A. Q. Huang, "Design and optimization of the high frequency transformer for a 800 V/1.2 MHz SiC LLC resonant converter," in *Proc. IEEE Energy Convers. Congr. Exposit. (ECCE)*, Oct. 2017, pp. 5317–5323.
[9] E. L. Barrios, A. Ursua, L. Marroyo, and P. Sanchis, "Analytical design methodology for litz-wired high-frequency power transformers," *IEEE Trans. Ind. Electron.*, vol. 62, no. 4, pp. 2103–2113, Apr. 2015.
[10] R. Wojda and M. Kazimierczuk, "Winding resistance of litz-wire and multi-strand inductors," *IET Pwr. Electr.*, vol. 5, no. 2, p. 257, 2012.
[11] J. Zhang, W. G. Hurley, and W. H. Wolfle, "Gapped transformer design methodology and implementation for LLC resonant converters," *IEEE Trans. Ind. Appl.*, vol. 52, no. 1, pp. 342–350, Jan. 2016.
[12] J. Zhang, W. G. Hurley, W. H. Wolfle, and M. C. Duffy, "Optimized design of LLC resonant converters incorporating planar magnetics," in *Proc. 28th Annu. IEEE Appl. Power Electron. Conf. Exposit. (APEC)*, no. 3, Mar. 2013, pp. 1683–1688.
[13] E. I. Amoiralis, M. A. Tsili, D. G. Paparigas, and A. G. Kladas, "Global transformer design optimization using deterministic and nondeterministic algorithms," *IEEE Trans. Ind. Appl.*, vol. 50, no. 1, pp. 383–394, Jan. 2014.
[14] J. R. Banumathy and R. Veeraraghavalu, "High frequency transformer design and optimization using bio-inspired algorithms," *Appl. Artif. Intell.*, vol. 32, nos. 7–8, pp. 707–726, Sep. 2018.

[15] L. Zhang, D. Zhang, H. Shui, Y. Yuan, Q. Pei, and J. Zhu, "Optimisation design of medium frequency transformer for the offshore dc grid based on multi-objective genetic algorithm," *IET Power Electron.*, vol. 10, no. 15, pp. 2157–2162, Dec. 2017.
[16] A. Garcia-Bediaga, I. Villar, L. Mir, I. Etxeberria-Otadui, and A. Rufer, "Novel multiobjective optimization of MF transformers for soft-switching converters using a genetic algorithm," in *Proc. 2014 IEEE Energy Convers. Congr. Exposit. (ECCE)*, Sep. 2014, pp. 5368–5375.
[17] M. Mogorovic and D. Dujic, "Medium frequency transformer design and optimization," in *Proc. Int. Conf. Power Electron., Intell. Motion, Renew. Energy Energy Manage. (PCIM)*, 2017, pp. 423–430.
[18] M. Mogorovic and D. Dujic, "100 kW, 10 kHz medium-frequency transformer design optimization and experimental verification," *IEEE Trans. Power Electron.*, vol. 34, no. 2, pp. 1696–1708, Feb. 2019.
[19] M. Mogorovic and D. Dujic, "Sensitivity analysis of medium-frequency transformer designs for solid-state transformers," *IEEE Trans. Power Electron.*, vol. 34, no. 9, pp. 8356–8367, Sep. 2019.
[20] M. Leibl, G. Ortiz, and J. W. Kolar, "Design and experimental analysis of a medium-frequency transformer for solid-state transformer applications," *IEEE J. Emerg. Sel. Topics Power Electron.*, vol. 5, no. 1, pp. 110–123, Mar. 2017.
[21] P. Shuai and J. Biela, "Design and optimization of medium frequency, medium voltage transformers," in *Proc. 15th Eur. Conference Power Electron. Appl. (EPE)*, Sep. 2013, pp. 1–10.
[22] W. G. Hurley and W. H. Wölfle, *Transformers and Inductors for Power Electronics: Theory, Design and Applications*, 1st ed. Chichester, U.K.: Wiley, pp. 123–157, 2013, ch. 5.
[23] M. K. Kazimierczuk, *High-Frequency Magnetic Components*, 2nd ed. Chichester, U.K.: Wiley, 2014, ch. 11, pp. 668–716.
[24] C. W. T. McLyman, *Transformer and Inductor Design Handbook*, 4th ed. New York, NY, USA: Taylor & Francis, 2011, chs. 6 7, pp. 224–253.
[25] R. W. Erickson and D. Maksimović, *Fundamentals of Power Electronics*, 2nd ed. Boston, MA, USA: Springer, 2004.
[26] Ferroxcube International Holding B.V, Ferroxcube. (2017). *Soft Ferrites and Accessories Data Handbook*. Accessed: Jun. 1, 2019. [Online]. Available: https://www.ferroxcube.com/en-global
[27] Tokin, A KEMET Company. (2017). *Ferrite Cores Catalogue, Tokin Electronic Components*. Accessed: Jun. 1, 2019. [Online]. Available: https://www.tokin.com/english/
[28] C. W. T. Mclyman. (2019). Magnetics 2017 Ferrite Cores Catalog. Magnetics Inc. Accessed: Jun. 1, 2019. [Online]. Available: https://www.mag-inc.com/
[29] F International, TSC Ferrite International Company. (2014). *A TSC International Company Ferrite Core Size/Shape Catalog*. Accessed: Jun. 1, 2019. [Online]. Available: http://www.tscinternational.com/mainferr.html
[30] ACME, ACME Electronics Corporation. (2018). *ACME Ferrite Cores Catalogue*. Accessed: Jun. 1, 2019. [Online]. Available: https://www.acme-ferrite.com.tw/en/ferrite.asp
[31] Y. Wang and D. Xiao, "Prototype design for a high-voltage high-frequency rectifier transformer for high power use," *IET Power Electr.*, vol. 4, no. 6, p. 615, 2011.
[32] F. Sedaghati, G. B. Gharehpetian, S. H. Hosseini, and M. Sabahi, "Extended configuration of dual active bridge DC–DC converter with reduced number of switches," *IET Power Electron.*, vol. 8, no. 3, pp. 401–416, Mar. 2015.
[33] Z. Yang, X. Gu, D. Kim, and Q. Yi, "Optimized design of high frequency transformer based on genetic algorithm," *Ind. Control Comput.*, vol. 30, no. 5, pp. 155–157, 2017.
[34] H. Karampoorian, G. Papi, and A. Zadehgol, "Volume and loss optimization of high frequency transformer for compact switch mode power supply considering corrected waveform factor," in *Proc. IEEE Power India Conf.*, 2006, pp. 27–32.
[35] M. O. Yuandong, M. O. Deyun, G. Mafeng, and L. Haishan, "The influence of magnetic core specification on the high frequency transformer performance of ultrasonic power supply," *J. Lingnan Norm. Univ.*, vol. 37, no. 6, pp. 44–50, 2016.
[36] F. Forest, E. Laboure, T. Meynard, and M. Arab, "Analytic design method based on homothetic shape of magnetic cores for high-frequency transformers," *IEEE Trans. Power Electron.*, vol. 22, no. 5, pp. 2070–2080, Sep. 2007.
[37] S. Salehahari, E. Babaei, S. H. Hosseini, and A. Ajami, "Transformer-based multilevel inverters: Analysis, design and implementation," *IET Power Electron.*, vol. 12, no. 1, pp. 1–10, Jan. 2019.
[38] N. R. Coonrod, "Transformer computer design aid for higher frequency switching power supplies," *IEEE Trans. Power Electron.*, vol. PE-1, no. 4, pp. 248–256, Oct. 1986.
[39] N. Mohan, T. M. Undeland, and W. P. Robbins, *Power electronics: Converters, Applications, and Design*, 3rd ed. New York, NY, USA: Wiley, 2003, ch. 30, pp. 744–792.
[40] R. Petkov, "Optimum design of a high-power, high-frequency transformer," *IEEE Trans. Power Electron.*, vol. 11, no. 1, pp. 33–42, Jan. 1996.
[41] W. Odendaal and J. Ferreira, "A thermal model for high-frequency magnetic components," *IEEE Trans. Ind. Appl.*, vol. 35, no. 4, pp. 924–931, 1999.
[42] D. Ahmed and L. Wang, "Optimal peak flux density model (OPFDM) for non-iterative design of high frequency gapped transformer (HFGT) in LLC resonant converters," *IET Power Electron.*, early access, Dec. 2019, doi: 10.1049/iet-pel.2019.0316.
[43] C. R. Sullivan and R. Y. Zhang, "Simplified design method for litz wire," in *Proc. IEEE Appl. Power Electron. Conf. Exposit. (APEC)*, Mar. 2014, pp. 2667–2674.
[44] T. L. Bergman, A. S. Lavine, and F. P. Incropera, *Fundamentals of Heat and Mass Transfer*, 7th ed. Hoboken, NJ, USA: Wiley, 2011.
[45] W. Shen, "Design of high-density transformers for high-frequency high-power converters," Ph.D. dissertation, Virginia Polytech. Inst. State Univ., Blacksburg, VA, USA, 2006.
[46] M. Mu and F. C. Lee, "A new core loss model for rectangular AC voltages," in *Proc. IEEE Energy Convers. Congr. Exposit. (ECCE)*, Sep. 2014, pp. 5214–5220.
[47] S. Yue, Y. Li, Q. Yang, X. Yu, and C. Zhang, "Comparative analysis of core loss calculation methods for magnetic materials under nonsinusoidal excitations," *IEEE Trans. Magn.*, vol. 54, no. 11, pp. 1–5, Nov. 2018.
[48] Y. Han and Y.-F. Liu, "A practical transformer core loss measurement scheme for high-frequency power converter," *IEEE Trans. Ind. Electron.*, vol. 55, no. 2, pp. 941–948, 2008.
[49] Y. Han, W. Eberle, and Y.-F. Liu, "A practical copper loss measurement method for the planar transformer in high-frequency switching converters," *IEEE Trans. Ind. Electron.*, vol. 54, no. 4, pp. 2276–2287, Aug. 2007.
[50] Texas Instruments. (2013). *400VDCin, 12V, PMP5967 LLC With Synchronous Rectifiers*. Accessed: Jun. 1, 2019. [Online]. Available: http://www.ti.com/tool/PMP5967

**DANIYAL AHMED** (Student Member, IEEE) was born in Islamabad, Pakistan, in 1987. He received the B.Sc. and M.Sc. degrees (Hons.) in electrical engineering from the University of Engineering and Technology (UET), Taxila, Pakistan, in 2009 and 2013, respectively. He is currently pursuing the Ph.D. degree with the Electrical Engineering Department, Nanjing University of Aeronautics and Astronautics, Nanjing, China.

His main research interests include optimized design and modeling of high-frequency magnetic components, high-frequency power conversion, wide-band-gap power semiconductor devices, and isolated dc–dc resonant converters.

**LI WANG** (Member, IEEE) received the B.E. and M.E. degrees in electrical engineering from the Henan University of Science and Technology, Luoyang, China, in 1990 and 1993, respectively, and the Ph.D. degree in electrical engineering from the Nanjing University of Aeronautics and Astronautics, Nanjing, China, in 2007.

She is currently a Professor with the Department of Electrical Engineering, College of Automation, Nanjing University of Aeronautics and Astronautics. She has authored or coauthored more than 100 articles and holds 29 national patents. Her current research interests include intelligent design, control, and protection in distribution microgrids, solid-state breaker, fault diagnosis, prognostics and health management in power systems, power conversion and management technology, and distribution network security.